The motion and deformation of a bubble in a Hele-Shaw cell

K. Wu[a],[1] D. J. Booth[a],[2] I. M. Griffiths[b],[2] P. D. Howell[b],[2] J. K. Nunes,[1] and H. A. Stone[b,1]

[1] *Department of Mechanical and Aerospace Engineering, Princeton University, Princeton, NJ 08544, USA*

[2] *Mathematical Institute, University of Oxford, Andrew Wiles Building, Oxford, OX2 6GG, UK*

(Dated: November 18, 2024)

We theoretically and experimentally study the propagation of a bubble in a Hele-Shaw cell under a uniform background flow at low Reynolds number. We consider situations where both the capillary number Ca and the ratio ϵ of the cell height to the bubble diameter are small. The bubble is then flattened into a pancake-like shape, with an approximately circular profile when viewed from above, and thin liquid films lie between the bubble and the cell walls. Bubble motion and deformation are determined by an interplay between the Hele-Shaw viscous pressure, the pressure drop due to the thin films, and the capillary pressure due to the in-plane curvature of the apparent bubble boundary. Numerical and asymptotic results indicate that, with all other parameters held constant, the in-plane aspect ratio of the bubble varies non-monotonically with its size, with smaller bubbles being flattened in the flow direction and larger bubbles being elongated. These theoretical predictions are validated experimentally, as well as the expected loss of fore-aft symmetry of the bubble shape due to differences between the advancing and retreating menisci. New measurements of the bubble velocity are also shown to agree well with theoretical predictions. We extend our results to describe a bubble moving in an inclined cell due to buoyancy. New experimental results for the bubble velocity, as well as results found in the literature, are shown to collapse under a scaling motivated by the theory. As in the case of a horizontal Hele-Shaw cell, we find that, with increasing bubble size, its shape can be switch from being flattened to elongated in the direction of motion.

I. INTRODUCTION

The flow of bubbles through a Hele-Shaw channel is ubiquitous in microfluidic experiments and applications [1–5]. In this work, we focus on the motion and deformation at low Reynolds number of an inviscid bubble in a channel whose height is small compared to the bubble's in-plane dimensions. The bubble is surrounded on all sides by liquid and separated from the cell walls by thin liquid films, therefore having a pancake-like shape [6].

[a] The first two authors contributed to this work equally

[b] Contact authors: ian.griffiths@maths.ox.ac.uk; howell@maths.ox.ac.uk; hastone@princeton.edu

Early progress in understanding the propagation of bubbles in Hele-Shaw channels proceeded from averaging over the depth of the channel and analyzing the resulting two-dimensional problem. It was first shown by Taylor and Saffman [7] that, in a regime where the capillary pressure at the bubble interface is effectively constant, a circular bubble in a Hele-Shaw channel travels at twice the speed of the background flow. Tanveer [8] analysed the deformation of a bubble in a Hele-Shaw channel using complex-variable methods and showed that, in the limit of large surface tension, the bubble is circular. Green *et al.* [9] numerically explored the effect of surface tension on the shape selection of a bubble in a Hele-Shaw cell with a uniform background flow. They found that, for each fixed value of the dimensionless surface tension, there exists a countably infinite number of possible shapes, one of which is always a circular bubble travelling at twice the background velocity. This work was extended by Lustri *et al.* [10] through the use of exponential asymptotics to solve the selection problem analytically in the limit that the dimensionless surface tension tends to zero. The effects of varying the geometry of the Hele-Shaw cell have also been studied, both experimentally and numerically. For example, exotic stable bubble shapes can be obtained by introducing a rail along the centre-line of a Hele-Shaw channel [11–13].

However, none of these works includes the effects of the thin liquid films above and below the bubble that are developed as the bubble travels through the cell. The formation of such liquid films was first reported by Bretherton [14], who studied an inviscid bubble moving through a viscous liquid in a capillary tube in the limit of small capillary number $\mathrm{Ca}_b = \hat{\mu}\hat{U}_b/\hat{\gamma}$, where $\hat{\mu}$ is the liquid viscosity, $\hat{U}_b$ is the bubble velocity, and $\hat{\gamma}$ is the liquid–air surface tension. Bretherton's analysis was formalised by Park and Homsy [15] using matched asymptotic expansions. For our purposes, their main finding is that viscous flow in the thin liquid films between the bubble and the cell walls causes an additional pressure jump across the bubble–liquid interface, which is proportional to $\mathrm{Ca}_b^{2/3}$. An effective boundary condition that includes this additional pressure jump was used by Meiburg [16] to study the effect on bubble shape. This approach was improved by Burgess and Foster [17] to capture correctly the Bretherton pressure drop at the rear interface of a moving bubble as well as to analyse inner regions where the velocity normal to the bubble interface is small and the Park and Homsy model [15] breaks down. Nagel [18] used the boundary condition proposed by Meiburg [16] to determine the velocity of an undeformable isolated viscous droplet and presented some numerical results for the velocity of a deformable droplet. Using the same boundary condition, a general model for the motion of bubbles in Hele-Shaw cells surrounded by thin liquid films was developed by Booth *et al.* [19], whose results will be extended in this work.

While all of the work mentioned previously has been concerned with pressure-driven flow in

a horizontal Hele-Shaw cell, there has also been significant progress in understanding the related problem of the rise of a bubble due to buoyancy in an inclined or vertical Hele-Shaw cell. A balance between viscous dissipation and work done by buoyancy is often used to relate the bubble velocity to the in-plane aspect ratio of the bubble and other physical parameters, while dissipation in the thin films is often neglected. Maxworthy [20] experimentally studied the shape and rise velocity of bubbles in an inclined Hele-Shaw cell and found that the bubbles elongate in the direction of motion. Eri and Okumura [21] studied bubbles rising in a vertical Hele-Shaw cell and likewise observed elongated bubble shapes. Monnet et al. [22] studied the effect of the Reynolds number on the shape and velocity of a rising bubble. For low Reynolds numbers, they found that the bubble is elongated in the direction of motion, whereas bubbles flattened in the direction of motion are characteristic of the inertial regime. We will show theoretically and experimentally that in fact both elongated and flattened bubbles are possible in buoyancy-driven flow at low Reynolds numbers.

The structure of this paper is as follows. In §II we present a model for the propagation and deformation of a bubble in a Hele-Shaw cell with a uniform background flow. The model contains two dimensionless parameters, the capillary number and the bubble aspect ratio, both of which are small for the work considered here, and we identify two possible distinguished asymptotic limits in which both of these parameters tend to zero. In §III we present numerical solutions to the model for general flow conditions. The experimental methodology is laid out in §IV, the results of which are analysed and compared to the model in §V. The model is then generalised to include buoyancy effects in §VI. We show that the experimental results of Maxworthy [20], Monnet *et al.* [22], and our own results collapse under a certain scaling. Finally, in §VII we summarise our key findings and discuss potential extensions to the modelling.

II. MATHEMATICAL MODELLING

A. Governing Equations

We consider a single bubble propagating in a Hele-Shaw cell parallel to the $(\hat{x}, \hat{y})$-plane. For the moment we assume that gravitational effects are negligible; this assumption is relaxed in §VI. Under the lubrication approximation, in the limit where the cell height $\hat{h}$ is much smaller than a

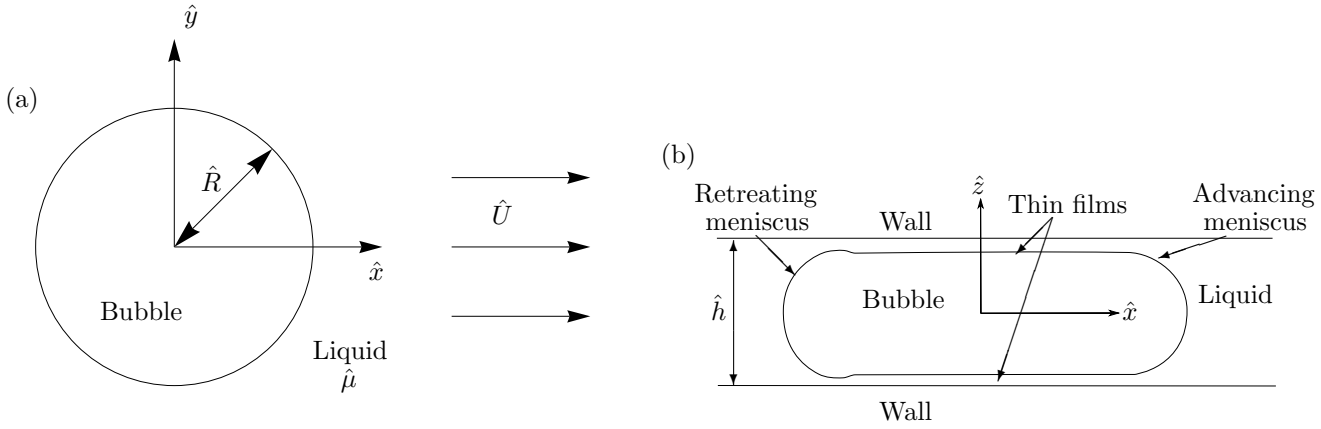

FIG. 1: (a) Plan view of a bubble in a Hele-Shaw cell with a uniform background flow of speed $\hat{U}$. (b) Side view of the bubble.

typical bubble radius $\hat{R}$, the flow away from the bubble is governed by the Hele-Shaw equations:

$$\hat{\boldsymbol{u}} = -\frac{\hat{h}^2}{12\hat{\mu}}\hat{\boldsymbol{\nabla}}\hat{p}. \tag{1a}$$

$$\hat{\boldsymbol{\nabla}} \cdot \hat{\boldsymbol{u}} = 0, \tag{1b}$$

where $\hat{\boldsymbol{u}}(\hat{x}, \hat{y})$ is the depth-averaged fluid velocity, $\hat{\mu}$ is the fluid viscosity, and $\hat{p}(\hat{x}, \hat{y})$ is the fluid pressure. The bubble is driven by a prescribed uniform background flow of speed $\hat{U}$ in the $\hat{x}$-direction (with corresponding unit vector $\boldsymbol{i}$), which leads to the far-field boundary condition

$$\hat{\boldsymbol{u}} \to \hat{U}\boldsymbol{i} \quad \text{as} \quad \hat{x}^2 + \hat{y}^2 \to \infty. \tag{2}$$

Looking down on the cell from above, the boundary of the bubble appears to be a closed curve in the $(\hat{x}, \hat{y})$-plane (see figure 1(a)), on which we impose the effective boundary conditions [16, 19]:

$$\boldsymbol{n} \cdot \hat{\boldsymbol{u}} = \hat{U}_n, \tag{3a}$$

$$\hat{p}_b - \hat{p} = \frac{2\hat{\gamma}}{\hat{h}} + \frac{2\hat{\gamma}}{\hat{h}}\,\beta(\mathrm{Ca}_n)\mathrm{Ca}_n^{2/3} + \frac{\hat{\gamma}\pi}{4}\hat{\kappa}. \tag{3b}$$

Here, $\boldsymbol{n}$, $\hat{U}_n$, and $\hat{\kappa}$ are the outward-pointing normal, normal velocity, and in-plane curvature of the apparent bubble boundary, respectively; $\hat{\gamma}$ is the surface tension, $\hat{p}_b$ is the uniform pressure inside the bubble, $\mathrm{Ca}_n = \hat{\mu}\hat{U}_n/\hat{\gamma}$ is the local capillary number based on the normal velocity, and β is the Bretherton coefficient, whose value depends on whether the meniscus is advancing or retreating

[14, 18, 23, 24]:

$$\beta(\mathrm{Ca}_n) = \begin{cases} \beta_1 \approx 3.88 & \text{when } \mathrm{Ca}_n > 0, \\ \beta_2 \approx -1.13 & \text{when } \mathrm{Ca}_n < 0. \end{cases} \tag{4}$$

The second term on the right-hand side of (3b) is the correction to the pressure difference, due to the thin-film regions between the bubble and the walls of the cell (see figure 1(b)), in the limit of small Ca_n [14]. We also require, however, that Ca_n is large enough so that film thicknesses are greater than molecular sizes and thus set by viscous effects and not disjoining pressure [2].

B. Non-dimensionalisation

We non-dimensionalise the system (1)–(3) by scaling lengths with the bubble radius $\hat{R}$, velocities with the far-field uniform flow velocity $\hat{U}$, and pressure with $12\hat{\mu}\hat{U}\hat{R}/\hat{h}^2$. Dimensionless quantities are represented without hats. Our dimensionless system is then given by:

$$\nabla^2 p = 0 \qquad \text{in} \quad \Omega, \tag{5a}$$

$$p_b - \frac{3\mathrm{Ca}}{\epsilon} p = 1 + \mathrm{Ca}^{2/3}\beta(U_n)U_n^{2/3} + \frac{\epsilon\pi}{4}\kappa \qquad \text{on} \quad \partial\Omega_b, \tag{5b}$$

$$\boldsymbol{n}\cdot\boldsymbol{\nabla} p = -U_n \qquad \text{on} \quad \partial\Omega_b, \tag{5c}$$

$$p \sim -x + o(1) \qquad \text{as} \quad x^2 + y^2 \to \infty, \tag{5d}$$

where Ω is the fluid domain and $\partial\Omega_b$ is the apparent bubble–fluid boundary in the (x, y)-plane, whose normal velocity is U_n. The system (5) contains two dimensionless parameters, the aspect ratio and the capillary number, defined by

$$\epsilon = \frac{\hat{h}}{2\hat{R}}, \qquad \mathrm{Ca} = \frac{\hat{\mu}\hat{U}}{\hat{\gamma}}, \tag{6a,b}$$

respectively.

One can show that the problem (5) has reflectional symmetry about the x-axis and thus that (in steady state) the bubble propagates in the x-direction. We can thus write

$$U_n = U_b \boldsymbol{i}\cdot\boldsymbol{n}, \tag{7}$$

where the bubble propagation speed U_b is to be determined. One can also show that the dimensionless bubble area is identically preserved by the system (5) and set equal to π by our choice of non-dimensionalisation. Also, the dimensionless bubble pressure p_b is then in principle determined as part of the solution.

By integrating (5b) around the bubble contour $\partial\Omega_b$ we obtain the identity

$$-\oint_{\partial\Omega_b} p\boldsymbol{n}\,\mathrm{d}s = \frac{\epsilon}{3\mathrm{Ca}^{1/3}}\oint_{\partial\Omega_b}\beta(U_n)U_n^{2/3}\boldsymbol{n}\,\mathrm{d}s, \tag{8}$$

which may be interpreted as a force balance on the bubble.

C. Complex variable formulation

Now we reformulate the problem (5) using complex variables. We define a complex potential w by $w(z)+U_b z = -p(x,y)+\mathrm{i}\psi(x,y)$, where ψ is the streamfunction and $z=x+\mathrm{i}y$. This function is holomorphic on Ω and satisfies the boundary conditions

$$\mathrm{Im}[w(z)] = 0 \qquad \text{on } \partial\Omega_b, \tag{9a}$$

$$p_b + \frac{3\mathrm{Ca}}{\epsilon}\,\mathrm{Re}[w(z)+U_b z] = 1+\frac{\pi\epsilon}{4}\kappa + \mathrm{Ca}^{2/3}\beta(U_n)U_n^{2/3} \qquad \text{on } \partial\Omega_b, \tag{9b}$$

$$w(z) \sim (1-U_b)z + o(1) \qquad \text{as } z\to\infty. \tag{9c}$$

By the Riemann Mapping Theorem, there exists a conformal map $z(\zeta)$ to the fluid region Ω from the unit disk $|\zeta|<1$, as shown schematically in figure 2. To fix the map uniquely, we take

$$z(\zeta) = \frac{a}{\zeta} + f(\zeta), \tag{10}$$

where $a\in\mathbb{R}_{>0}$, $f(\zeta)$ is holomorphic in $|\zeta|<1$ and, without loss of generality, we choose $f(0)=0$. Note that this choice does not, in general, imply that the centroid of the bubble is at the origin, but that can be fixed *a posteriori*. The assumed symmetry about the real axis implies that f satisfies

$$f(\overline{\zeta}) = \overline{f(\zeta)}, \tag{11}$$

where the bar denotes complex conjugation. Equivalently, if f is expanded in the Taylor series

$$f(\zeta) = \sum_{n=1}^{\infty} c_n\zeta^n, \tag{12}$$

then the coefficients c_n are all real.

In the ζ-plane, the boundary conditions for $W(\zeta)=w(z(\zeta))$ can be derived from (9) to give

$$\mathrm{Im}[W(\zeta)] = 0 \qquad \text{on} \quad |\zeta|=1, \tag{13a}$$

$$p_b + \frac{3\mathrm{Ca}}{\epsilon}\,\mathrm{Re}[W(\zeta)+U_b z(\zeta)] = \frac{\pi\epsilon}{4}\kappa + \mathrm{Ca}^{2/3}\beta(U_n)U_n^{2/3} \qquad \text{on} \quad |\zeta|=1, \tag{13b}$$

$$W(\zeta) \sim \frac{a(1-U_b)}{\zeta} + o(1) \qquad \text{as} \quad \zeta\to 0. \tag{13c}$$

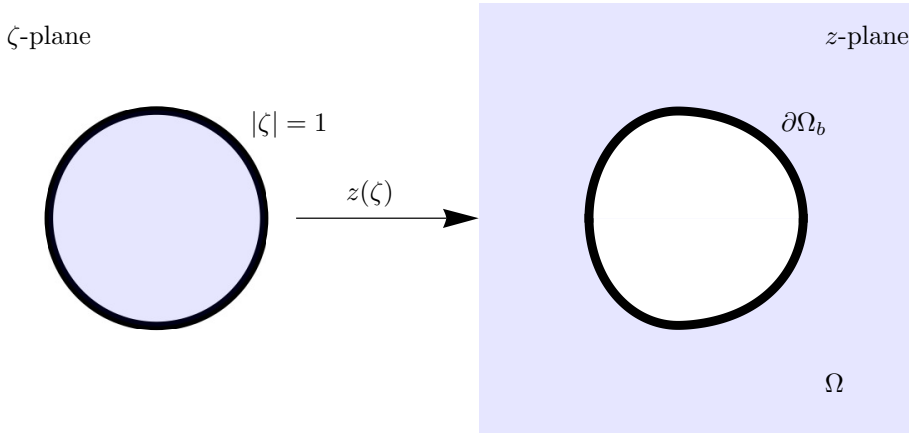

FIG. 2: Schematic of the conformal map $z(\zeta)$ from the unit disk $|\zeta| < 1$ to the fluid region, Ω, in the z-plane.

We observe that

$$W(\zeta) = a(1 - U_b)\left(\zeta + \frac{1}{\zeta}\right) \tag{14}$$

satisfies (13a) and (13c). It only remains to impose the dynamic boundary condition (13b), which can be expressed as

$$\kappa = \frac{4}{\epsilon\pi}(p_b - 1) + \frac{12\mathrm{Ca}}{\epsilon^2\pi}\,\mathrm{Re}\left[(2 - U_b)a\zeta + U_b f(\zeta)\right] - \frac{4\mathrm{Ca}^{2/3}U_b^{2/3}}{\pi\epsilon}\beta(\boldsymbol{i}\cdot\boldsymbol{n})|\boldsymbol{i}\cdot\boldsymbol{n}|^{2/3}, \tag{15a}$$

on $|\zeta| = 1$, with

$$\kappa = -\frac{1}{|z'(\zeta)|}\left(1 + \mathrm{Re}\left[\frac{\zeta z''(\zeta)}{z'(\zeta)}\right]\right), \tag{15b}$$

$$\boldsymbol{i}\cdot\boldsymbol{n} = -\frac{\mathrm{Re}[\zeta z'(\zeta)]}{|z'(\zeta)|}, \tag{15c}$$

where $'$ denotes differentiation.

In principle, if a were known, then (15a) would provide a boundary condition that uniquely determines the holomorphic function f from which we can find the bubble shape. As previously mentioned, we fix the translation by setting $f(0) = 0$. Then to close the system we impose the area constraint

$$\frac{1}{2\pi\mathrm{i}}\oint_{|\zeta|=1} z\left(\frac{1}{\zeta}\right) z'(\zeta)\,\mathrm{d}\zeta = -1, \tag{16}$$

which, by the use of Cauchy's Residue Theorem, reduces to

$$a = 1 + \frac{1}{2\pi\mathrm{i}}\oint_{|\zeta|=1} f\left(\frac{1}{\zeta}\right) f'(\zeta)\,\mathrm{d}\zeta, \tag{17}$$

or, in terms of the series expansion (12),

$$a = 1 + \sum_{n=1}^{\infty} n c_n^2. \tag{18}$$

Thus the *a priori* unknown constant a is in principle determined. The force balance (8) may be expressed as

$$\oint_{|\zeta|=1} \kappa z'(\zeta)\,\mathrm{d}\zeta = 0. \tag{19}$$

Upon substituting (15a) this condition reduces to

$$\frac{12\mathrm{iCa}}{\epsilon^2}\big((2-U_b)a(c_1-a)+U_b(a-1-ac_1)\big) = \frac{4\mathrm{Ca}^{2/3}U_b^{2/3}}{\epsilon\pi}\oint_{|\zeta|=1}\beta(\boldsymbol{i}\cdot\boldsymbol{n})|\boldsymbol{i}\cdot\boldsymbol{n}|^{2/3}\left(-\frac{a}{\zeta^2}+f'(\zeta)\right)\mathrm{d}\zeta. \tag{20}$$

The right-hand side is not easily expressible in general, but (20) in principle determines the bubble velocity, U_b.

Finally, for any physically relevant solution the bubble boundary, $\partial\Omega_b$, is a simple closed curve, so

$$2\pi = \oint_{\partial\Omega}\kappa\,\mathrm{d}s = \oint_{|\zeta|=1}\frac{\kappa|z'(\zeta)|}{\mathrm{i}\zeta}\,\mathrm{d}\zeta, \tag{21}$$

which in principle determines p_b.

D. Distinguished limits

1. *Dominant balances*

We return to the dynamic boundary condition (15a), with the individual terms now labeled for clarity:

$$\underbrace{\kappa}_{①} = \underbrace{\frac{4}{\epsilon\pi}(p_b-1)}_{②} + \underbrace{\frac{12\mathrm{Ca}}{\epsilon^2\pi}\,\mathrm{Re}\left[(2-U_b)a\zeta+U_b f(\zeta)\right]}_{③} - \underbrace{\frac{4\mathrm{Ca}^{2/3}U_b^{2/3}}{\pi\epsilon}\beta(\boldsymbol{i}\cdot\boldsymbol{n})|\boldsymbol{i}\cdot\boldsymbol{n}|^{2/3}}_{④}. \tag{22}$$

The aspect ratio ϵ and capillary number Ca are both small parameters. The dominant balance in (22) depends on their relative sizes, and there are two distinguished limits to consider.

1. $\mathrm{Ca} = O(\epsilon^3)$: the viscous pressure (term 3) balances the pressure drop due to the thin films (term 4).

2. $\mathrm{Ca} = O(\epsilon^2)$: the viscous pressure (term 3) balances the curvature (term 1).

In both distinguished limits we find that $p_b \sim 1 + O(\epsilon)$, indicating that the leading-order bubble pressure is determined by the capillary pressure jump across the meniscus.

2. *Distinguished limit 1:* $\mathrm{Ca} = O(\epsilon^3)$

The leading-order problem in this limit was solved by Booth *et al.* [19], who defined the Bretherton parameter

$$\delta = \frac{1}{\eta}\frac{\mathrm{Ca}^{1/3}}{\epsilon} = O(1) \tag{23}$$

as ϵ and Ca both tend to zero, where

$$\eta = \frac{(\beta_1 - \beta_2)\Gamma(4/3)}{3\sqrt{\pi}\Gamma(11/6)} \approx 0.894 \tag{24}$$

is a numerical constant. We may interpret the Bretherton parameter δ as a dimensionless parameter that compares the relative contributions of the viscous pressure and the Bretherton pressure in the normal stress balance (5b), which scale with Ca/ϵ and $\mathrm{Ca}^{2/3}$, respectively. In the limit $\delta \to \infty$, the viscous pressure dominates over the Bretherton pressure and *vice versa* in the limit $\delta \to 0$. Since $\delta \propto \hat{R}/\hat{h}$, we note that δ serves as a proxy for the bubble size when all other parameters are held constant.

From (15a) we find that the leading-order curvature is constant, so the bubble boundary is a unit circle at leading order. It follows from (17) that the mapping function must take the form

$$z(\zeta) \sim \frac{1}{\zeta} + \epsilon f_1(\zeta) + O(\epsilon^2). \tag{25}$$

We also expand the bubble velocity, U_b in powers of ϵ, as

$$U_b \sim U_0 + \epsilon U_1 + O(\epsilon^2). \tag{26}$$

In this regime we find that the leading-order bubble velocity is determined as a function of δ by

$$\frac{U_0^{2/3}}{2 - U_0} = \delta. \tag{27}$$

This formula for the velocity of an isolated circular bubble was found in [19]. The extension of this result to compute the $O(\epsilon)$ perturbations to the shape (i.e. $f_1(\zeta)$) and the bubble velocity U_1 can be found in §A 1. These are found analytically and we find that $f_1(\zeta) \propto U_0^{2/3}$ and U_1 is solely a function of U_0.

3. *Distinguished limit 2:* $\mathrm{Ca} = O(\epsilon^2)$

In this regime, $\delta = O(\epsilon^{-1/3})$, and the viscous pressure and curvature (terms 3 and 1, respectively, in (22)) balance at leading order. The resulting leading-order problem is well studied, and it has been shown that the only stable solution is a circular bubble that moves at twice the background flow velocity (see, for example, [10]). We perturb about this leading-order solution by expanding the mapping function and bubble velocity as

$$z(\zeta) \sim \frac{1}{\zeta} + \epsilon^{1/3} f_2(\zeta) + O\left(\epsilon^{2/3}\right), \qquad U_b \sim \tilde{U}_0 + \epsilon^{1/3}\tilde{U}_1 + O\left(\epsilon^{2/3}\right). \tag{28a,b}$$

At leading order, we find that $\tilde{U}_0 = 2$. The details of the asymptotic analysis to compute the $O(\epsilon^{1/3})$ perturbations to the shape (i.e. $f_2(\zeta)$) and the bubble velocity $\tilde{U}_1$ can be found in §A 2. Again, these are found analytically and they are functions of $C = \mathrm{Ca}/\epsilon^2$.

III. NUMERICAL SIMULATIONS

A. Numerical formulation

In this section we calculate numerical solutions of (5) for general values of ϵ and Ca, following the methodology laid out in [9]. We expand the bubble shape function $f(\zeta)$ as a truncated Taylor series

$$f(\zeta) \approx \sum_{n=1}^{N-1} c_n \zeta^n, \tag{29}$$

where we recall that the $N-1$ coefficients, c_n, are all real due to the symmetry condition (11). In addition to $\{c_n\}$, we have to solve for U_b, p_b and a, so in total we need $N+2$ equations to form a closed system. We obtain the first equation by enforcement of the bubble area constraint (18), and the other $N+1$ equations we acquire by evaluating (15a) at $N+1$ points along the upper half circle, namely $p_j = \mathrm{e}^{\pi j/N}$ for $0 \le j \le N$. Note that any physical solution will automatically satisfy the relations (19) and (21). The resulting system of $N+2$ algebraic equations is solved using Newton's method. The convergence of the series (29) is determined by the convergence of the Taylor series of $\beta(\boldsymbol{i}\cdot\boldsymbol{n})|\boldsymbol{i}\cdot\boldsymbol{n}|^{2/3}$, which is non-analytic (cf. (A5) and (A6)), implying that $c_n = O(n^{-5/3})$ as $n \to \infty$.

In general, we have two parameters, Ca and ϵ, which may be varied independently. We plot the results versus the Bretherton parameter, $\delta = \mathrm{Ca}^{1/3}/\eta\epsilon$, with either ϵ held constant while Ca is varied or *vice versa*.

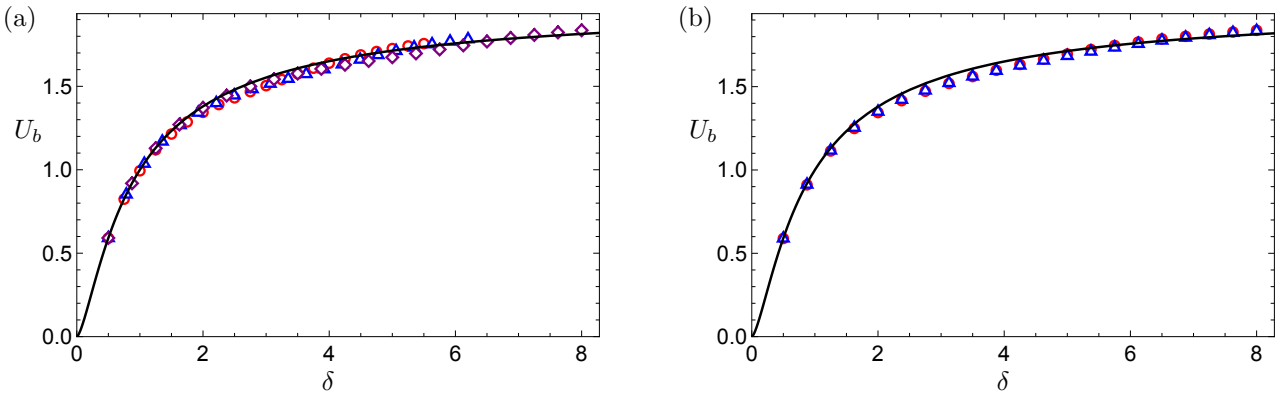

FIG. 3: Dimensionless bubble velocity U_b versus Bretherton parameter δ. The theoretical prediction (27) is shown as a black curve, and numerical simulations of (5) are shown as points. (a) Fixed $\epsilon = 0.05$ (red circles), 0.025 (blue triangles), 0.01 (purple diamonds); (b) fixed $\mathrm{Ca} = 6.7 \times 10^{-4}$ (red circles), 3.3×10^{-4} (blue triangles).

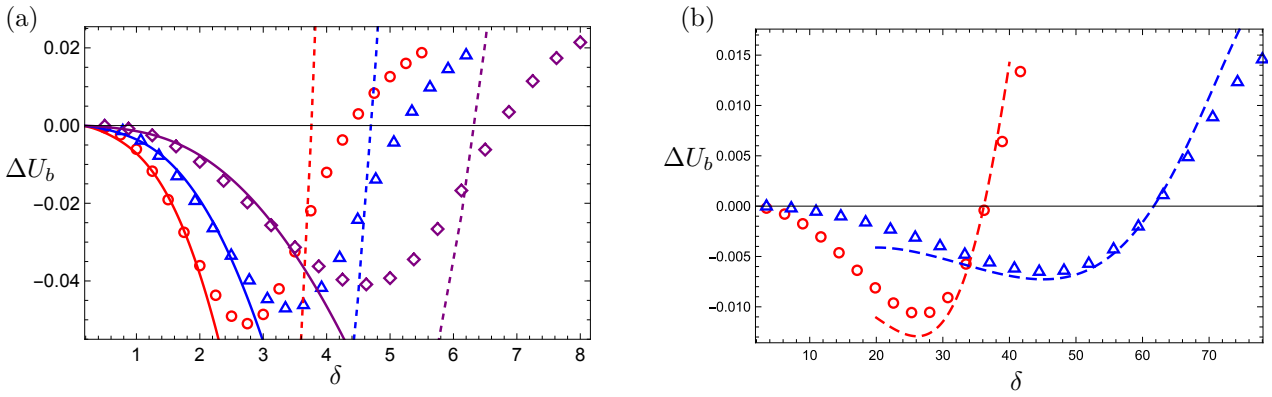

FIG. 4: The difference ΔU_b (30) between the numerically calculated bubble velocity U_b and the leading-order prediction (27) versus δ. (a) Fixed $\epsilon = 0.05$ (red circles), 0.025 (blue triangles), 0.01 (purple diamonds); (b) fixed $\epsilon = 5 \times 10^{-5}$ (red), 10^{-5} (blue). Also shown are asymptotic predictions for the distinguished limits given by (26) when $\mathrm{Ca} = O(\epsilon^3)$ ($\delta = O(1)$, solid curves) and (28) when $\mathrm{Ca} = O(\epsilon^2)$ ($\delta = O(\epsilon^{-1/3})$, dashed curves).

B. Results

In figure 3 we plot the dimensionless bubble velocity versus δ, keeping ϵ constant in figure 3(a), and Ca constant in figure 3(b). In all cases the numerical results are observed to follow the theoretical prediction (27) closely. The value of U_b is over-predicted by (27) when δ is small and under-predicted when δ is large. To see this trend more clearly, we calculate

$$\Delta U_b = U_b - U_0, \tag{30}$$

where U_b is the numerical solution for the bubble velocity and U_0 is the asymptotic approximation that satisfies equation (27). We define ΔU_b in this manner to compare the true bubble velocity with the prediction obtained by assuming that the bubble is circular. We plot ΔU_b versus δ in figure 4 with ϵ held constant; similar qualitative behaviour is observed with Ca held constant. As $\delta \to 0$ the approximation (27) becomes perfect. Then, as δ is increased, the difference transitions from (27) over-predicting to under-predicting the bubble velocity.

Alongside the numerical results we plot the asymptotic results discussed previously in §II. In figure 4(a) we find that the distinguished limit where $\mathrm{Ca} = O(\epsilon^3)$ (see §II D 2) accurately predicts the initial over-prediction of (27) for small δ. The second distinguished limit (see §II D 3) correctly predicts that, as δ increases, (27) changes from over-predicting to under-predicting the bubble velocity, as seen in the numerical solutions. In figure 4(a) we observe a large difference between the asymptotic solution in distinguished limit 2 and the numerical solution. This discrepancy is due to the range of values of ϵ chosen, with the smallest being $\epsilon = 0.01$, for which $\epsilon^{1/3} \approx 0.2$. In figure 4(b), we plot ΔU_b for $\epsilon = 5 \times 10^{-5}$, and $\epsilon = 10^{-5}$ (so $\epsilon^{1/3} \approx 0.04$ and ≈ 0.02, respectively). We observe convergence of the numerical and asymptotic solutions with decreasing ϵ and much closer agreement than seen in figure 4(a).

We plot the computed bubble shapes for different values of δ in figure 5. For small values of δ, figure 5(a) illustrates that the bubble shape is flattened in the x-direction (the direction of propagation). In figure 5(b) it is shown that, as δ is increased, the bubble shape evolves from being flattened in the x-direction to being elongated. In figures 5(a) and 5(b), we observe that there is fore-aft asymmetry, which is due to the different values of β depending on whether the meniscus is advancing or retreating (4). Bubble shapes tend to be wider towards the rear and narrower towards the front.

To quantify these results, we define the in-plane aspect ratio as

$$A = \frac{z(1) - z(-1)}{2 \max_{|\zeta|=1} \left\{ |\operatorname{Im}[z(\zeta)]| \right\}}. \tag{31}$$

In figure 6, the in-plane aspect ratio A is plotted versus δ and indeed we observe that the bubble shape changes from being flattened ($A < 1$) to elongated ($A > 1$) as δ is increased. We find that the crossover points where $A = 1$ approximately match the values of δ where $\Delta U_b = 0$ in figure 4. This observation suggests that the discrepancies observed in figure 3 can be attributed to bubble deformation, with flattened bubbles moving slower than predicted and elongated bubbles travelling faster.

Asymptotic results for the in-plane aspect ratio are also plotted in figure 6(a). In the first

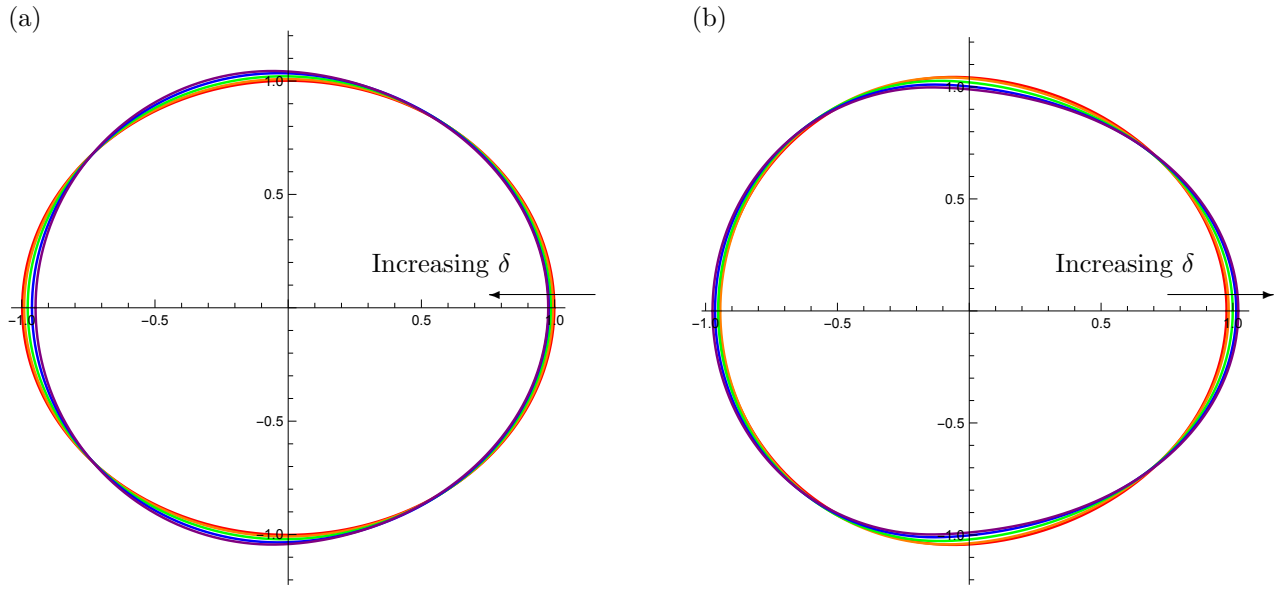

FIG. 5: Numerical solutions for the bubble shape with fixed $\epsilon = 0.05$. Flow is from left to right. In (a), $\delta = 0.5$ (red), 1 (orange), 1.5 (green), 2 (blue), 2.5 (purple). In (b) $\delta = 2.5$ (red), 3 (orange), 3.5 (green), 4 (blue), 4.5 (purple).

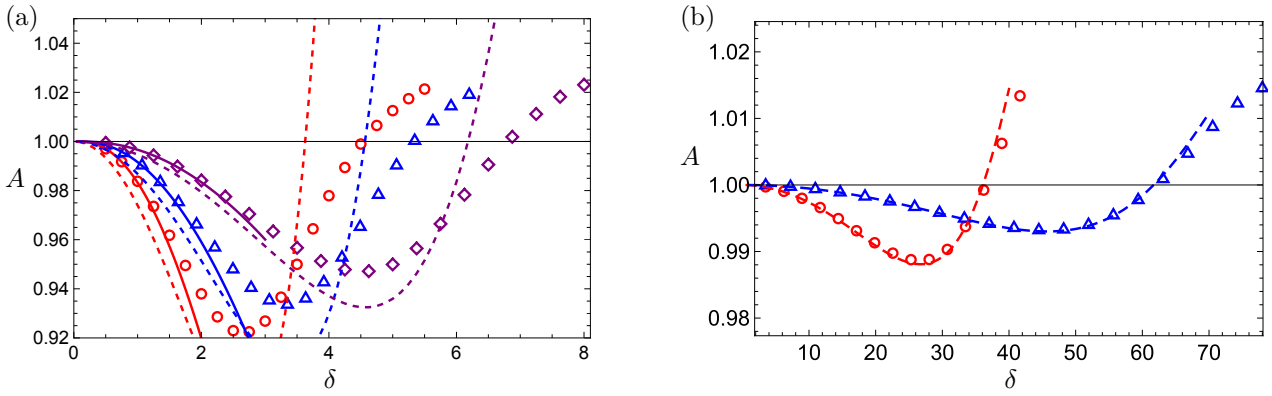

FIG. 6: Numerically computed in-plane bubble aspect ratio A, defined by (31), versus δ. (a) Fixed $\epsilon = 0.05$ (red circles), 0.025 (blue triangles), 0.01 (purple diamonds); (b) fixed $\epsilon = 5 \times 10^{-5}$ (red), 10^{-5} (blue). Also shown are asymptotic predictions for the distinguished limits $\mathrm{Ca} = O(\epsilon^3)$, where $\delta = O(1)$ (solid curves) and $\mathrm{Ca} = O(\epsilon^2)$, where $\delta = O(\epsilon^{-1/3})$ (dashed curves).

distinguished limit, $\mathrm{Ca} = O(\epsilon^3)$, we accurately predict the initial flattening of the bubble shape in the flow direction. The second distinguished limit $\mathrm{Ca} = O(\epsilon^2)$ captures the non-monotonicity of the in-plane bubble aspect ratio, with the bubbles being flattened for small values of δ, and becoming elongated for larger values of δ. In figure 6(b) we plot the in-plane bubble aspect ratio, A, for $\epsilon = 5 \times 10^{-5}$ and $\epsilon = 10^{-5}$ (so $\epsilon^{1/3} \approx 0.04$ and ≈ 0.02, respectively). As in figure 4, we

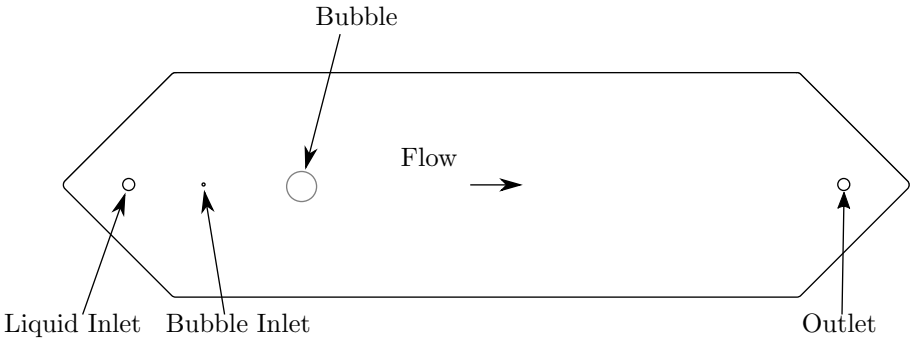

FIG. 7: Diagram of the Hele-Shaw cell including a bubble of typical size.

observe convergence of the numerical and asymptotic solutions with decreasing ϵ, and much closer agreement than seen in figure 6(a).

IV. EXPERIMENTAL METHODS

Experiments were performed in a Hele-Shaw cell constructed using two 12.7 mm thick cast acrylic plates. A section shaped like an elongated hexagon was sealed by a gasket along its perimeter, and a uniform distance between the plates was maintained using plastic spacers. The plan view layout of the cell is shown in figure 7.

Flow in the channel was manipulated using a series of circular holes cut into the top plate. Liquid was injected into and removed from the cell through 4 mm diameter holes whose centres were located at opposing vertices of the hexagon. Bubbles were manually introduced using a syringe connected to a 1 mm diameter hole located downstream of the main inlet. The bubble inlet was sealed when not in use to limit fluctuations in pressure and flow rate during measurements. The components of the cell were cleaned with ethanol and distilled water prior to assembly and experiments. Cells of two different geometries were used. In the first, the cell height was $\hat{h} = 0.29\,\text{mm}$, the width was $\hat{w} = 90\,\text{mm}$, and the length of the rectangular section was 19 cm. In the second, the cell height was $\hat{h} = 0.42\,\text{mm}$, the width was $\hat{w} = 65\,\text{mm}$, and the length of the rectangular section was 22 cm.

The viscous liquid used in experiments was silicone oil (Sigma Aldrich, Product No. 317667) that had a kinematic viscosity of $\hat{\nu} = 5\,\text{mm}^2/\text{s}$, a dynamic viscosity of $\hat{\mu} = 4.6\,\text{mPa s}$, and a surface tension of $\hat{\gamma} = 18.2\,\text{mN/m}$. The bubbles were composed of air. Flow was generated by driving oil into the cell at a constant volumetric flow rate, $\hat{Q}$, through the liquid inlet using a syringe pump (Harvard Apparatus, PHD Ultra). Oil ejected from the cell was collected, filtered, then reused.

Experiments were recorded using a DSLR camera (Nikon) positioned to capture the plan view

$\hat{h}$ [μm]	$\hat{U}$ [mm/s]	Ca $\times 10^4$	$\hat{R}$ [mm]	$\epsilon \times 10^2$	δ	px/mm
290	1.3	3.3	0.59–14.0	1–25	0.3–7.5	54
290	2.6	6.6	0.57–11.0	1–25	0.4–7.4	54
420	1.6	4.1	1.1–5.8	3–20	0.4–2.3	17
420	2.4	6.1	1.1–6.8	3–18	0.5–3.1	17

TABLE I: Experimental parameters: the cell height $\hat{h}$, the depth-averaged background flow velocity $\hat{U}$, the capillary number $\mathrm{Ca} = \hat{\mu}\hat{U}/\hat{\gamma}$, the effective bubble radius $\hat{R}$, the bubble aspect ratio $\epsilon = \hat{h}/2\hat{R}$, the Bretherton parameter $\delta = \mathrm{Ca}^{1/3}/\eta\epsilon$, and image resolution reported in pixels per mm.

of the Hele-Shaw cell. The cell was illuminated from above, and a light-absorbing black background was used to enhance contrast. Reflections of light from the bubble interfaces caused the plan view shapes of the bubbles to appear as white outlines. Videos were acquired at 30 frames per second. Images were calibrated using an object of known size in the focal plane.

For the purposes of measuring bubble velocities, bubble locations were tracked by fitting ellipses onto their outlines in the images. Bubble shapes were extracted by obtaining an array of points on the closed contour on which the pixel intensity was maximized in grey-scale images. The radius of a circle of equivalent area for each bubble was used as the effective radius of the bubble for scaling and further data reduction. In all cases, the ratio of the effective radius to the width of the channel was less than 0.16. Blockage effects due to the presence of the bubble were not taken into account, and the background flow velocity was estimated to be $\hat{U} = \hat{Q}/\hat{w}\hat{h}$. Reynolds numbers $\mathrm{Re} = 2\hat{U}\hat{R}\epsilon^2/\hat{\nu}$ ranged from 7.9×10^{-4} to 3.9×10^{-2}. Experimental parameters for the data sets reported in the following section are tabulated in table I.

V. RESULTS

We plot the prediction (27) for the dimensionless bubble velocity U_b versus the Bretherton parameter δ, alongside results of the experiments, in figure 8. We observe very good agreement between theory and experiments, including in the previously unstudied regime where $\delta < 1$. The experimental results support the predicted transition of the bubble speed from slower than to faster than the outer flow as δ increases through 1.

In the experiments, the bubble boundary $\partial\Omega_b$ is captured as a set of points $\{(x_i, y_i) : i =$

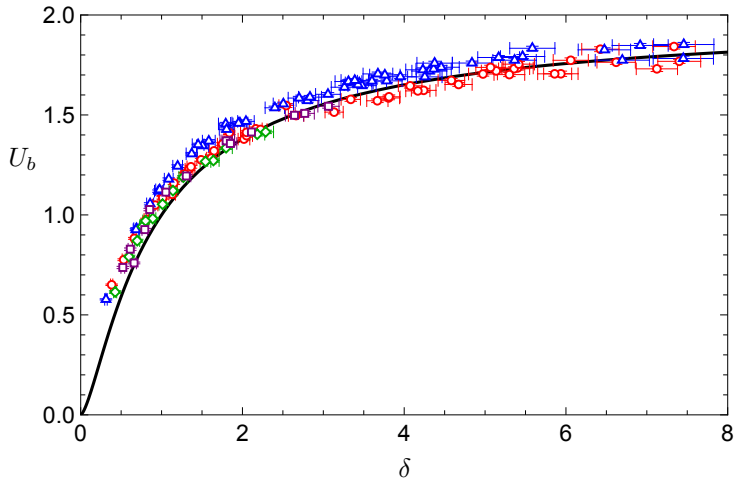

FIG. 8: The ratio U_b of the bubble velocity to the outer fluid velocity as a function of the Bretherton parameter δ. The solid curve shows the model prediction (27). The points show experimental data: (red circles) $\mathrm{Ca} = 6.6 \times 10^{-4}$, (blue triangles) $\mathrm{Ca} = 3.3 \times 10^{-4}$, (green diamonds) $\mathrm{Ca} = 4.1 \times 10^{-4}$, and (purple squares) $\mathrm{Ca} = 6.1 \times 10^{-4}$ with the aspect ratio ϵ in the range 0.01–0.25.

$1, \cdots, N\}$, and the in-plane aspect ratio is then calculated using

$$A = \frac{\max |x_i - x_j|}{\max |y_i - y_j|}. \tag{32}$$

In figure 9, we plot the measured in-plane aspect ratio versus the Bretherton parameter, δ, for two fixed values of the capillary number. The corresponding numerically computed in-plane aspect ratios are plotted as solid curves. We observe good agreement for small values of δ. The experiments confirm the theoretically predicted non-monotonic behaviour of the bubble shape, and the transition from being flattened to being elongated in the direction of the flow, as δ increases.

For large values of δ, the experiments document a linear increase in the in-plane aspect ratio A, whereas the theory predicts that A saturates to a constant. In this limit, we expect the theory to start to break down, because the bubble develops a prominent fore-aft asymmetry. To account for this asymmetry, we would need to incorporate the full boundary condition found in [17], where the value of β_2 varies along the rear meniscus as a function of $\mathrm{Ca}_n^+/\mathrm{Ca}_n^-$, where $\mathrm{Ca}_n^\pm$ are the capillary numbers based on the normal velocity at corresponding points on the front and rear bubble interfaces. We have also neglected the influence of the leakage of liquid through the thin films, which will be discussed in §VII. Both of these effects may contribute to the much sharper rise in the in-plane aspect ratio A observed in experiments than predicted by our theory.

We show in figure 10 experimentally measured bubble shapes, compared with the numerical so-

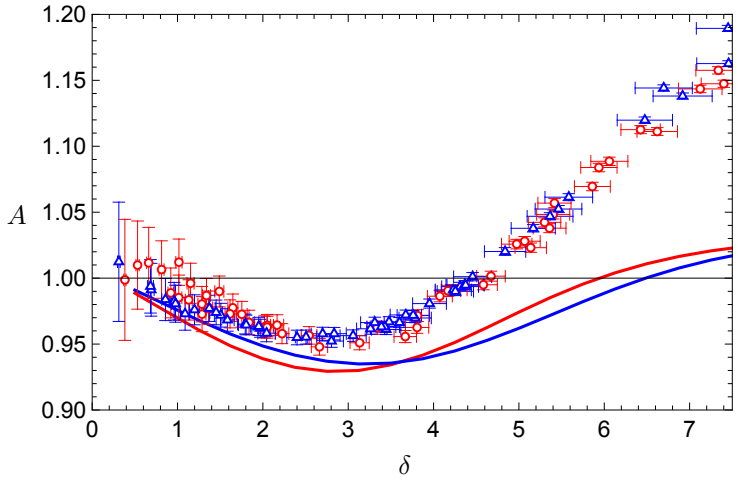

FIG. 9: In-plane aspect ratio, A, of the bubble, versus δ with capillary number fixed at $\mathrm{Ca} = 6.6 \times 10^{-4}$ (red circles), and $\mathrm{Ca} = 3.3 \times 10^{-4}$ (blue triangles). The points show experimental measurements and curves show numerically computed values given by (31).

lutions at the same flow conditions. Again, we see good agreement between theory and experiments for small values of δ. As δ is increased, the theory correctly predicts the direction of deformation and the fore-aft asymmetry of the bubble shape, though the bubbles in the experiments are elongated in the flow direction more than suggested by the theory. In figure 11 we plot the position of the bubble centroid x_c relative to the bubble midpoint $x_m$versus δ. We observe that $x_c - x_m$ is generally less than zero, which reflects the observation that bubble shapes are wider towards the rear. There is good agreement between the experimental and numerical results, indicating that the degree of fore-aft asymmetry is predicted well by our theory. We notice that $x_c - x_m \neq 0$ when $A = 1$ in figure 9, hence the bubble is not circular at the crossover between flattening and elongation. The agreement between numerical and experimental results for $x_c - x_m$ in figure 11 is perhaps unexpected considering the discrepancy between measured and predicted in-plane aspect ratios A in figure 9 for the same range of δ. We interpret this finding to be a sign that the degree of asymmetry between the rear and front menisci remains approximately constant even as factors not included in our model affect the flattening or elongation of the bubble.

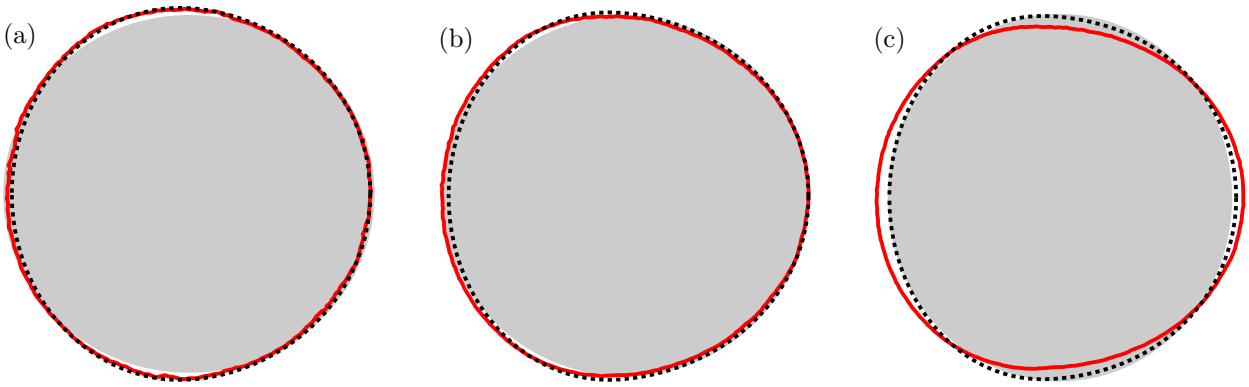

FIG. 10: Experimental bubble shapes (red solid), numerical solutions (black dashed), and the unit circle (grey fill). Flow is from left to right. For $\delta =$ (a) 2.66, (b) 4.67, (c) 7.12, with $\mathrm{Ca} = 6.6 \times 10^{-4}$.

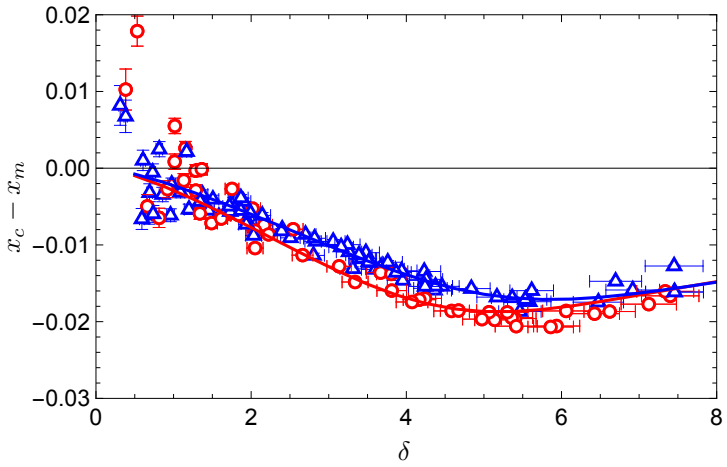

FIG. 11: The location of the bubble centroid x_c relative to the bubble midpoint x_m versus δ with capillary number fixed at $\mathrm{Ca} = 6.6 \times 10^{-4}$ (red circles), and $\mathrm{Ca} = 3.3 \times 10^{-4}$ (blue triangles). The points show experimental measurements and curves show numerically computed values.

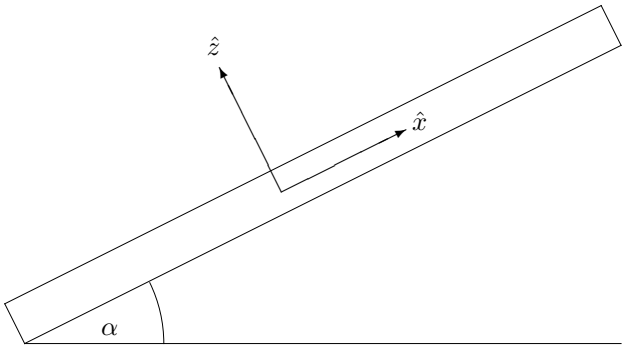

FIG. 12: Side view of a Hele-Shaw cell inclined at an angle α to the horizontal.

Source	$\hat{h}$ [mm]	α [°]	Ca $\times 10^3$	$\epsilon \times 10^2$	δ
Maxworthy [20]	1.8	3.6–18.9	3.8–20	2–96	0.2–7.5
Monnet et al. [22]	{2, 2.3}	90	37–51	4–181	0.2–9.8
Current work	0.29	7.5	0.23	1–18	0.4–5.7

TABLE II: Experimental parameters for bubbles rising due to buoyancy: the cell height $\hat{h}$, the inclination angle α, the capillary number $\mathrm{Ca} = \hat{h}^2\hat{\rho}\hat{g}\sin\alpha/24\hat{\gamma}$, the bubble aspect ratio $\epsilon = \hat{h}/2\hat{R}$, and the Bretherton parameter $\delta = \mathrm{Ca}^{1/3}/\eta\epsilon$. Maxworthy does not report the density of the silicone oil used in his experiments, so a typical value $\hat{\rho} = 0.960\,\mathrm{g/mL}$ was used, based on silicone oils with similar kinematic viscosity (e.g., Sigma-Aldrich product nos. 378364 and 378356). Monnet et al. present velocity data scaled using the in-plane aspect ratio χ (A in our notation). Based on their figure 4, we took $\chi = 1.2$ when rescaling.

VI. BUOYANCY-DRIVEN FLOW

A. Velocity of a rising bubble

Many Hele-Shaw cell experiments study the rise of a bubble due to buoyancy, such as those presented by Maxworthy [20] and Monnet et al. [22]. We consider purely buoyancy-driven flow in a Hele-Shaw cell inclined at an angle α to the horizontal (see figure 12). We non-dimensionalise the bubble velocity with a characteristic buoyancy velocity $\hat{\rho}\hat{g}\hat{h}^2\sin\alpha/24\hat{\mu}$, where $\hat{\rho}$ and $\hat{g}$ are the fluid density and the acceleration due to gravity, respectively. Then we define the effective capillary number to be $\mathrm{Ca} = \hat{\rho}\hat{g}\hat{h}^2\sin\alpha/24\hat{\gamma}$. Using these definitions, we find that the leading-order dimensionless bubble velocity

$$U_b = \frac{24\hat{\mu}\hat{U}_b}{\hat{\rho}\hat{g}\hat{h}^2\sin\alpha} \tag{33}$$

satisfies exactly the same equation (27) as for a purely pressure-driven bubble. The details of the mathematical modelling can be found in Appendix B.

B. Experiments for buoyancy-driven flow

Measurements of buoyancy-driven bubbles were acquired using the cell of height $\hat{h} = 0.29\,\mathrm{mm}$, width $\hat{w} = 90\,\mathrm{mm}$, and the rectangular section of length 19 cm. There was no background flow, and the cell was inclined at an angle of $\alpha = 7.5°$, which produced a capillary number of $\mathrm{Ca} = 2.3\times10^{-4}$. In the reported measurements, the effective bubble radii ranged from $\hat{R} = 0.8\,\mathrm{mm}$ to $\hat{R} = 12.1\,\mathrm{mm}$,

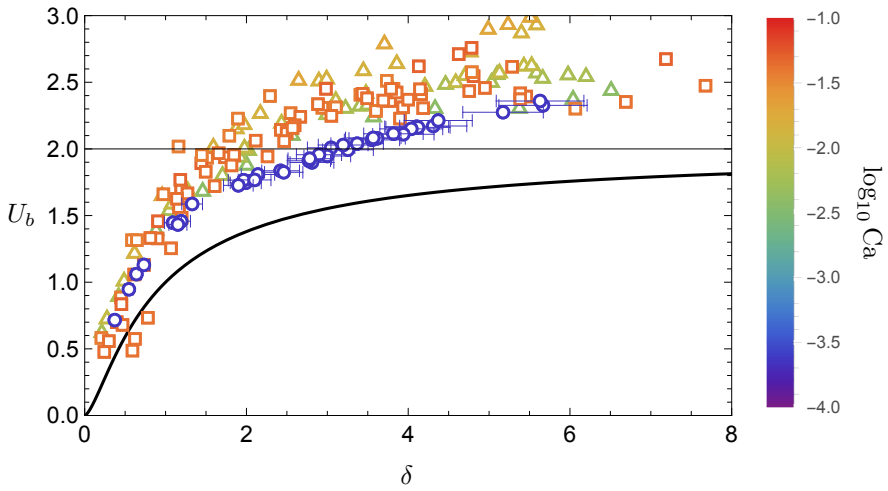

FIG. 13: Relative bubble velocity U_b as a function of Bretherton parameter, δ. Experimental data are shown from our experiments (circles), from Maxworthy [20] (triangles), and from Monnet *et al.* [22] (squares). The model prediction (27) is represented by a black curve. The colour bar shows $\log_{10}$ Ca.

corresponding to an aspect ratio ϵ in the range 0.01–0.18 and Bretherton parameter δ in the range 0.4–5.7. Reynolds numbers calculated using the characteristic buoyancy velocity in place of the background flow velocity were in the range 3.1×10^{-4} to 4.8×10^{-3}.

Where appropriate, we compare our results with data from the experiments of Maxworthy [20] and of Monnet et al. [22]. A summary of the relevant parameters for each of the experimental datasets is provided in table II. Detailed information about bubble shape was not available. In cases where an in-plane aspect ratio was provided, the effective radius was estimated by approximating the bubble shape as an ellipse.

C. Results for buoyancy-driven bubbles

In figure 13 we plot the normalised velocity U_b of a buoyancy-driven bubble versus the Bretherton parameter δ. Data from our experiments are shown alongside rescaled data from Maxworthy [20] and Monnet et al. [22]. The three datasets, which collectively span a wide range of heights $\hat{h}$, inclination angles α, and capillary numbers Ca, collapse under the scalings that we have presented in this study, in particular when plotted against the dimensionless group

$$\delta \propto \left(\frac{\hat{\rho}\hat{g}\hat{R}^3 \sin\alpha}{\hat{\gamma}\hat{h}} \right)^{1/3}. \tag{34}$$

It is especially notable that the data collapse across such a large range of capillary numbers, suggesting that the model for the Bretherton pressure drop, which assumes $\mathrm{Ca}^{1/3} \ll 1$, is sufficiently accurate up to $\mathrm{Ca} = O(10^{-1})$ or possibly greater.

Although the collapse of the experimental results is encouraging, we find that the theoretical prediction (27) (shown as a black curve) significantly under-predicts the bubble velocity (though the qualitative behaviour is similar). This observation is in contrast with the pressure-driven case shown in figure 8. The nature of this discrepancy suggests that the rise velocity is underestimated by Maxworthy's prediction $U_b = 2$ for a circular bubble (attained in the limit $\delta \to \infty$ in our theory). Both Maxworthy [20] and Monnet et al. [22] argue that elongated bubbles should travel faster than circular bubbles and accordingly multiply by the in-plane aspect ratio to adapt the expected rise velocity for an elliptical bubble shape. Such adjustments to the bubble rise velocity based on the bubble shape are not included in the simple model (27). Nonetheless, our model helps to explain the observed behaviour, including the monotonic increase up to an approximately constant rise velocity as δ becomes large and the associated deviation from Maxworthy's prediction $U_b = 2$ for smaller δ.

The discrepancies between the predictions of our model and experimental measurements could be attributed to a number of other factors. For example, we have neglected gravitational effects on the capillary-static meniscus at the bubble boundary. Suresh & Grotberg [25] show that, at $O(1)$ values of the Bond number $\mathrm{Bo} = 24\mathrm{Ca}/\sin\alpha$, gravitational effects modify the Bretherton coefficients $\beta_{1,2}$. Other possible contributors are discussed in §VII.

In figure 14, we plot experimental results for the in-plane aspect ratio, A, of a buoyancy-driven bubble from our experiments and from Maxworthy [20], versus the Bretherton parameter, δ. As for a pressure-driven bubble (figure 8), we observe non-monotonic behaviour, whereby the bubble flattens in the direction of motion for small values of δ and elongates for larger values of δ. The in-plane aspect ratios from our experiments and from those of Maxworthy [20] reach as high as $A = 1.3$ at around $\delta = 6$, and the trends indicate that even higher values could be obtained as δ is increased further. The in-plane aspect ratios reported by Monnet et al. [22] in their figure 4 occupy a similar range, $A \approx 1.2$, for bubbles in the viscous regime. However, we do not reproduce them here because, due to the manner in which their data is presented, it is difficult to extract individual data points and to obtain precise values of the in-plane aspect ratio and of measures of bubble size in the regime of interest to us. Although there is a reasonable collapse in the data, we observe that a weak dependence on Ca remains. This dependence of in-plane aspect ratio on capillary number also helps to rationalise observations about the collapse of the scaled bubble velocities in figure 13.

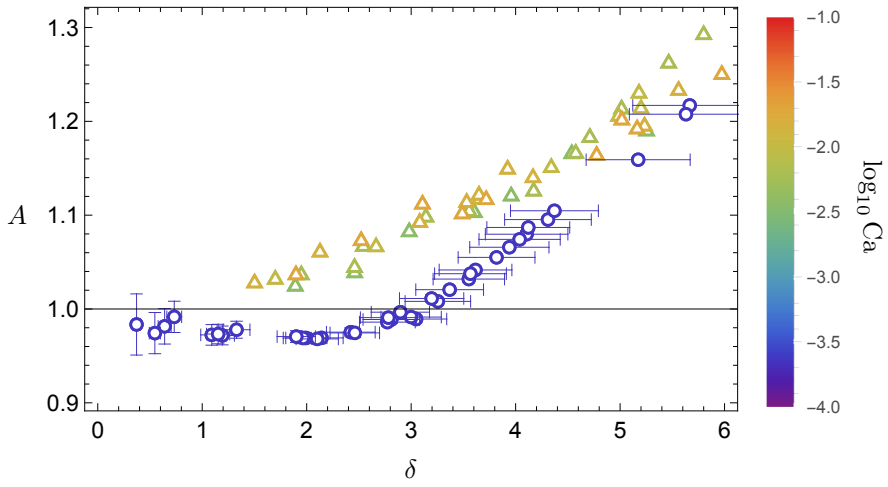

FIG. 14: In-plane aspect ratio, A, as a function of Bretherton parameter, δ, for a buoyancy-driven bubble from our experiments (circles) and from Maxworthy [20] (triangles). The colour bar shows $\log_{10}\mathrm{Ca}$.

In particular, the scaled velocities from our experiments are generally smaller than those from the experiments of Maxworthy [20] and Monnet et al. [22]. This trend may be expected considering the positive correlation between in-plane bubble aspect ratio and expected rise velocity for purely buoyancy-driven bubbles, since their experiments were performed at significantly higher values of Ca than ours, by a factor of $\approx$ 20–200 (see table II).

VII. CONCLUSIONS AND EXTENSIONS

In this article we present new experimental results and extend the theoretical results of [19] for the flow of an isolated bubble in a Hele-Shaw cell with a uniform background velocity. The mathematical model depends on two dimensionless parameters, the bubble aspect ratio ϵ and the capillary number Ca, both of which are assumed to be small. We identify two asymptotic distinguished limits in which either (1) $\mathrm{Ca} = O\left(\epsilon^3\right)$ or (2) $\mathrm{Ca} = O\left(\epsilon^2\right)$ as both ϵ and Ca tend to zero. In either case, the bubble is circular to leading order, and we obtain the first corrections to both the bubble velocity and the bubble shape. In Limit 1, we reproduce the leading-order solution (27) found by [19], which determines the bubble velocity as a function of the Bretherton parameter $\delta \propto \mathrm{Ca}^{1/3}/\epsilon = O(1)$, and we find that the bubble flattens in the direction of motion as δ increases from zero. In Limit 2, we find that the bubble travels at approximately twice the background flow speed, and predict that the bubble switches from being flattened to being elongated in the flow direction with increasing δ.

New experimental results for the bubble velocity (see figure 8) are found to agree well with the theoretical prediction (27). These results also validate the prediction of [19] that the bubble moves faster than the fluid speed for $\delta > 1$ and slower for $\delta < 1$, the latter being a regime previously unstudied in the literature. The bubble shapes were also captured experimentally. Strikingly, we find that the in-plane aspect ratio of the bubble varies non-monotonically with δ, with the bubble first flattening then elongating in the direction of motion as δ is increased. Furthermore, a loss of fore-aft symmetry in the bubble shape, due to the differences in the advancing and retreating menisci (included in the model through the Bretherton coefficients (4)), is both predicted and experimentally observed.

Numerical simulations are shown to agree with the theoretical prediction (27) of the bubble velocity and to reproduce the non-monotonicity of the in-plane aspect ratio seen in experiments (see figure 9). For small δ, the numerical results agree well with the experiments, but for larger δ the experiments see more pronounced deformations than the theory predicts. This discrepancy is theorised to be due to the variation of the Bretherton coefficients in (4) due to the variation of the normal direction at the rear meniscus.

We extend our results to describe a bubble moving through an inclined cell due to buoyancy. New experimental data for the rise velocity of a buoyancy-driven bubble are found to collapse with the prior data of Maxworthy [20] and Monnet et al. [22] when plotted against δ (see figure 13) and follow the same trend as the prediction (27). However, the experimental results depart significantly from the theoretical prediction that the normalised rise velocity should follow the same dependence (27) on δ as for a pressure-driven bubble. We hypothesise that this discrepancy could be reduced by including the variation of the Bretherton parameters in (4) with respect to the Bond number [25]. Similarly to the pressure-driven results, we observe that the in-plane aspect ratio of the bubble is non-monotonic as δ is varied, again initially flattening in the direction of gravity (in the cell) and elongating for larger values of δ.

Finally, we discuss how the model could be extended to more accurately model the effects of the thin liquid films above and below the bubble and potentially improve the theoretical prediction of the bubble deformation. We have already noted that the effects of fore-aft asymmetry in the bubble shape and of gravity on the menisci at the bubble boundary could be included by generalising the simple model (4) for the Bretherton coefficients. It is also true that many experiments in the literature are at relatively large capillary numbers where the accuracy of Bretherton's approximation

(4) is uncertain. Many studies [26–29] have extended the ideas to larger values of Ca_n using

$$\beta \sim \frac{\beta_1}{1 + 5.7\mathrm{Ca}_n^{2/3}} \quad \text{when } \mathrm{Ca}_n > 0, \tag{35}$$

which they obtained by matching the original Bretherton result [14] with numerical results by Reinelt & Saffman [30]. While these papers do not present a corresponding result for the retreating meniscus, in principle a similar expression could be found by the same procedure, allowing us to extend the validity of our results to larger values of Ca.

We also note that the kinematic boundary condition (3a) ignores the flow of liquid through the thin films. As shown in [17, 28], one can adapt (5c) to include these effects, giving

$$-\boldsymbol{n} \cdot \nabla p = U_n \left(1 - 1.34\mathrm{Ca}_n^{2/3}\right). \tag{36}$$

Preliminary numerical experiments suggest that this modification slightly improves the agreement between theory and experiment, but not enough to reproduce the sharp increase in the in-plane aspect ratio observed, e.g., in figure 9.

ACKNOWLEDGMENTS

DJB is grateful to EPSRC, grant reference number EP/V520202/1, for funding. KW gratefully acknowledges the support of the National Science Foundation Graduate Research Fellowship under Grant No. DGE-2039656.

Appendix A: Asymptotic analysis

1. Distinguished limit 1: $\mathrm{Ca} = O(\epsilon^3)$

a. Asymptotic expansions

With the bubble shape mapping function given by (25), we calculate

$$\kappa \sim 1 + \epsilon\,\mathrm{Re}\left[(\zeta^3 f_1'(\zeta))'\right] + O(\epsilon^2), \tag{A1a}$$

$$\boldsymbol{i} \cdot \boldsymbol{n} \sim \mathrm{Re}[\zeta] + \frac{\epsilon}{2}\,\mathrm{Re}[(\zeta^3 - \zeta) f_1'(\zeta)] + O(\epsilon^2). \tag{A1b}$$

Furthermore, we expand the remaining variables in powers of ϵ as

$$\frac{4}{\epsilon\pi}(p_b - 1) \sim 1 + \frac{4\epsilon}{\pi} p_{b_2} + O(\epsilon^2), \tag{A2a}$$

$$U_b \sim U_0 + \epsilon U_1 + O(\epsilon^2). \tag{A2b}$$

b. Shape perturbations

The dynamic boundary condition (15a) at $O(\epsilon)$ gives

$$\mathrm{Re}\left[(\zeta^3 f_1'(\zeta))'\right] = \frac{4}{\pi}p_{b_2} + \frac{12\delta^3\eta^3}{\pi}(2-U_0)\,\mathrm{Re}[\zeta] - \frac{4\delta^2\eta^2 U_0^{2/3}}{\pi}\beta\,(\mathrm{Re}[\zeta])\,|\,\mathrm{Re}[\zeta]|^{2/3}. \tag{A3}$$

We can then read off

$$(\zeta^3 f_1'(\zeta))' = \frac{4}{\pi}p_{b_2} + \frac{12\delta^3\eta^3}{\pi}(2-U_0)\zeta - \frac{4\delta^2\eta^2 U_0^{2/3}}{\pi}\,b(\zeta), \tag{A4}$$

where

$$b(\zeta) = \frac{b_0}{2} + \sum_{n=1}^{\infty} b_n \zeta^n, \tag{A5}$$

is holomorphic in $|\zeta|<1$, such that $\mathrm{Re}[b(\mathrm{e}^{\mathrm{i}\theta})] = \beta(\cos\theta)|\cos\theta|^{2/3}$. The coefficients b_n are given by

$$b_n = \frac{\Gamma\left(\frac{5}{3}\right)\Gamma\left(\frac{n}{2}-\frac{1}{3}\right)}{4\pi 2^{2/3}\Gamma\left(\frac{n}{2}+\frac{4}{3}\right)}\Bigg[\left((\sqrt{3}+1)\beta_1 + (\sqrt{3}-1)\beta_2\right)(-1)^{\lfloor\frac{n-1}{2}\rfloor} - \left((\sqrt{3}-1)\beta_1 + (\sqrt{3}+1)\beta_2\right)(-1)^{\lfloor\frac{n}{2}\rfloor}\Bigg]. \tag{A6}$$

Since f_1 is holomorphic in $|\zeta|<1$ we require the linear and constant terms to vanish on the right hand side of (A4). We thus find that the bubble pressure p_{b_2} is given by

$$p_{b_2} = \frac{\delta^2\eta^2 U_0^{2/3} b_0}{2} = \frac{\delta^2\eta^2 U_0^{2/3}\Gamma(5/6)(\beta_1+\beta_2)}{2\sqrt{\pi}\Gamma(4/3)}, \tag{A7a}$$

and the leading-order bubble velocity, U_0, satisfies

$$\frac{\delta(2-U_0)}{U_0^{2/3}} = \frac{(\beta_1-\beta_2)\Gamma(4/3)}{3\sqrt{\pi}\eta\Gamma(11/6)} = 1, \tag{A7b}$$

which reduces to (27).

We then integrate (A4) to find

$$f_1(\zeta) = -\frac{4\delta^2\eta^2 U_0^{2/3}}{\pi}\sum_{n=1}^{\infty}\frac{b_{n+1}\zeta^n}{n(n+2)}, \tag{A8}$$

which determines the $O(\epsilon)$ shape perturbations. The in-plane bubble aspect ratio may be expanded in the form

$$\begin{aligned} A &\sim 1 + \frac{\epsilon}{2}\big(f_1(1) - f_1(-1) + \mathrm{i}f_1(-\mathrm{i}) - \mathrm{i}f_1(\mathrm{i})\big) \\ &= 1 - \frac{8\epsilon\delta^2\eta^2 U_0^{2/3}}{\pi}\sum_{k=1}^{\infty}\frac{b_{4k+2}}{(4k+1)(4k+3)}. \end{aligned} \tag{A9}$$

c. *Asymptotics of the Bretherton integral*

Next we analyse how the shape perturbations affect the bubble velocity by expanding the force balance (20) up to $O(\epsilon)$. To evaluate the integral on the right-hand side, we need to understand the asymptotic behaviour of $\beta(\boldsymbol{i}\cdot\boldsymbol{n})|\boldsymbol{i}\cdot\boldsymbol{n}|^{2/3} = \mathrm{Re}[b(\mathrm{e}^{\mathrm{i}\theta})]$, where $\boldsymbol{n} = (\cos\theta, \sin\theta)$. Then we have

$$\mathrm{e}^{\mathrm{i}\theta} = -\frac{\zeta z'(\zeta)}{|z'(\zeta)|} \sim \frac{1}{\zeta}\left(1 - \epsilon \mathrm{i}\,\mathrm{Im}[\zeta^2 f_1'(\zeta)]\right) + O(\epsilon^2), \tag{A10}$$

and thus

$$\beta(\boldsymbol{i}\cdot\boldsymbol{n})|\boldsymbol{i}\cdot\boldsymbol{n}|^{2/3} \sim \mathrm{Re}[b(\zeta)] - \epsilon\,\mathrm{Im}[\zeta^2 f_1'(\zeta)]\,\mathrm{Im}[\zeta b'(\zeta)] + O(\epsilon^2). \tag{A11}$$

This expansion allows us to find that the asymptotic behaviour of the integral on the right-hand side of the force balance (20) is given by

$$\begin{aligned}\oint_{|\zeta|=1} \beta(\boldsymbol{i}\cdot\boldsymbol{n})|\boldsymbol{i}\cdot\boldsymbol{n}|^{2/3}\left(-\frac{a}{\zeta} + f'(\zeta)\right)\mathrm{d}\zeta \\ \sim -\oint_{|\zeta|=1} \mathrm{Re}[b(\zeta)]\frac{\mathrm{d}\zeta}{\zeta^2} + \epsilon\oint_{|\zeta|=1}\left\{\mathrm{Re}[b(\zeta)]f_1'(\zeta) + \frac{1}{\zeta^2}\,\mathrm{Im}[\zeta^2 f_1'(\zeta)]\,\mathrm{Im}[\zeta b'(\zeta)]\right\}\mathrm{d}\zeta. \\ \sim -\mathrm{i}\pi b_1 + \frac{\epsilon}{4}\oint_{|\zeta|=1}\Big(2\zeta b(\zeta) + (1+\zeta^2)b'(\zeta)\Big)f_1'\left(\frac{1}{\zeta}\right)\frac{\mathrm{d}\zeta}{\zeta^3},\end{aligned} \tag{A12}$$

by Cauchy's Residue Theorem. Finally using (A8) and Cauchy's Residue Theorem once again we find that the integral at $O(\epsilon)$ is given by

$$\begin{aligned}\frac{1}{4}\oint_{|\zeta|=1}\Big(2\zeta b(\zeta) + (1+\zeta^2)b'(\zeta)\Big)f_1'\left(\frac{1}{\zeta}\right)\frac{\mathrm{d}\zeta}{\zeta^3} &= -2\mathrm{i}\delta^2\eta^2 U_0^{2/3}\sum_{n=1}^{\infty} b_{n+1}(b_n + b_{n+2}) \\ &= -\mathrm{i}\left(\frac{96\Gamma(2/3)}{7\sqrt{\pi}\Gamma(1/6)} - \frac{27}{5\pi}\right)(\beta_1^2 - \beta_2^2)\delta^2\eta^2 U_0^{2/3}.\end{aligned} \tag{A13}$$

d. *Velocity perturbation*

We are now in position to find the velocity perturbation. We note from (A8) that the first Taylor coefficient in f is given by

$$c_1 \sim -\frac{4\delta^2\eta^2 U_0^{2/3} b_2}{3\pi}\,\epsilon + O\left(\epsilon^2\right). \tag{A14}$$

By using (A12) and (A13), we can therefore expand the force balance equation (20) as

$$\begin{aligned}\frac{3\eta\delta}{U_0^{2/3}}(U_0 - 2) + \epsilon\delta\eta\left(\frac{6(1-U_0)}{U_0^{2/3}}\,\frac{c_1}{\epsilon} + \frac{4+U_0}{U_0^{5/3}}U_1\right) \\ \sim -b_1 - \epsilon\left(\frac{96\Gamma(2/3)\sqrt{\pi}}{7\Gamma(1/6)} - \frac{27}{5}\right)\frac{(\beta_1^2 - \beta_2^2)}{\pi^2}\delta^2\eta^2 U_0^{2/3} + O(\epsilon^2).\end{aligned} \tag{A15}$$

At leading order, equation (A15) is satisfied identically, and the velocity perturbation is found at $O(\epsilon)$ to be given by

$$U_1 = -\frac{(\beta_1^2-\beta_2^2)U_0^{7/3}}{\pi^2(4+U_0)}\left\{\left(\frac{96\Gamma(2/3)\sqrt{\pi}}{7\Gamma(1/6)}-\frac{27}{5}\right)-\frac{4\cdot 2^{2/3}\sqrt{3}(\beta_1-\beta_2)\Gamma(-2/3)\Gamma(4/3)^2}{25\pi^2}\frac{U_0^{2/3}(U_0-1)}{(2-U_0)^2}\right\}. \tag{A16}$$

2. Distinguished limit 2: $\mathrm{Ca} = O(\epsilon^2)$

a. Asymptotic expansions

In this regime, we let $\mathrm{Ca} = C\epsilon^2$, where $C = O(1)$. The mapping function f and bubble velocity U_b are expanded as in equation (28), and we also expand the bubble pressure in the form

$$\frac{4}{\epsilon\pi}(p_b-1) \sim 1+\frac{4\epsilon^{1/3}}{\pi}p_{b_2}+O\left(\epsilon^{2/3}\right). \tag{A17}$$

b. Shape perturbations

In this limit, the dynamic boundary condition (15a) becomes

$$1+\epsilon^{1/3}\,\mathrm{Re}[(\zeta^3 f_2'(\zeta))'] \sim 1+\frac{4\epsilon^{1/3}}{\pi}p_{b_2}+\frac{12C\epsilon^{1/3}}{\pi}\,\mathrm{Re}[2f_2(\zeta)-\tilde{U}_1\zeta] - \epsilon^{1/3}\frac{4C^{2/3}2^{2/3}}{\pi}\beta(\mathrm{Re}[\zeta])|\,\mathrm{Re}[\zeta]|^{2/3}+O\left(\epsilon^{2/3}\right). \tag{A18}$$

This equation is identically satisfied at leading order. At $O\left(\epsilon^{1/3}\right)$ we read off

$$(\zeta^3 f_2'(\zeta))' = \frac{4}{\pi}p_{b_2}+\frac{12C}{\pi}(2f_2(\zeta)-\tilde{U}_1\zeta)-\frac{4C^{2/3}2^{2/3}}{\pi}b(\zeta), \tag{A19}$$

where $b(\zeta)$ is holomorphic in $|\zeta|<1$ and is given by the Taylor series (A5).

Since $f_2(\zeta)$ is holomorphic in $|\zeta|<1$ we expand it as a Taylor series, namely

$$f_2(\zeta) = \sum_{n=1}^{\infty} d_n\zeta^n, \tag{A20}$$

where $c_n = \epsilon^{1/3}d_n$. Substituting this series into (A19), we find that the constant term determines the bubble pressure,

$$p_{b_2} = \frac{C^{2/3}b_0}{2^{1/3}}. \tag{A21}$$

Then the linear term gives

$$\begin{aligned}\tilde{U}_1 &= -\frac{2^{2/3}b_1}{3C^{1/3}} + 2d_1, \\ &= -\frac{2^{2/3}\eta}{C^{1/3}} + 2d_1,\end{aligned} \tag{A22}$$

which in principle determines the velocity perturbation. Note that the first term on the right-hand side of (A22) is equivalent to the $O(\epsilon^{1/3})$ correction obtained by expanding (27) when $\delta = C^{1/3}/\eta\epsilon^{1/3}$; thus, this term is the correction to the velocity assuming the bubble is circular. Then, the second term is the correction to the bubble velocity due to the deviation of the bubble's shape from circular. Evaluating at subsequent powers of ζ we find the recurrence relation

$$d_n - \frac{\pi}{24C}(n^2-1)d_{n-1} = \frac{2^{2/3}b_n}{6C^{1/3}}. \tag{A23}$$

The general solution of (A23) for d_n grows factorially for large n, violating our assumption that the Taylor series (A20) converges inside the unit disk. We deduce that the only acceptable solution of (A23) is given by

$$d_n = -\frac{2^{2/3}}{6C^{1/3}}(n+1)!(n-1)!\sum_{j=0}^{\infty}\frac{b_{n+j+1}}{(n+j+2)!(n+j)!}\left(\frac{24C}{\pi}\right)^{j+1}, \tag{A24}$$

for $n \geq 1$. The in-plane aspect ratio of the bubble may then be expanded in the form

$$A \sim 1 + 2\epsilon^{1/3}\sum_{k=0}^{\infty} d_{4k+1}. \tag{A25}$$

c. Velocity perturbation

The velocity perturbation is found from (A22) and (A24), giving

$$\tilde{U}_1 = -\frac{2^{5/3}}{3C^{1/3}}\sum_{j=0}^{\infty}\frac{b_{j+1}}{j!(j+2)!}\left(\frac{24C}{\pi}\right)^{j}, \tag{A26}$$

where b_n is given by (A6). Thus the velocity perturbation is determined as a function of $C = \mathrm{Ca}/\epsilon^2$.

Appendix B: Buoyancy-driven flow

1. Model setup

We consider a bubble propagating in a Hele-Shaw cell of thickness $\hat{h}$ parallel to the $(\hat{x}, \hat{y})$-plane, inclined at an angle α to the horizontal (see figure 12). Under the lubrication approximation, in

the limit where $\hat{h}$ is much smaller than the radius of the bubble, the flow away from the bubble is still governed by the Hele-Shaw equations (1), where now $\hat{p}(\hat{x},\hat{y})$ is the modified pressure such that

$$\hat{p}(\hat{x},\hat{y}) = \hat{P}(\hat{x},\hat{y}) + \hat{\rho}\hat{g}\hat{x}\sin\alpha, \tag{B1}$$

where $\hat{P}$ is the fluid pressure, and $\hat{\rho}$ and $\hat{g}$ are the fluid density and acceleration due to gravity, respectively.

a. Dimensionless problem

After incorporating buoyancy into (1)–(3), we non-dimensionalise as follows (in which dimensionless variables are denoted without hats),

$$\begin{aligned}
&(\hat{x},\hat{y}) = \hat{R}(x,y), \quad (\hat{\boldsymbol{u}},\hat{U}_n) = \left(\hat{U} + \frac{\hat{\rho}\hat{g}\hat{h}^2\sin\alpha}{24\hat{\mu}}\right)(\boldsymbol{u},U_n),\\
&(\hat{p},\hat{P}) = \frac{12\hat{\mu}\hat{R}}{\hat{h}^2}\left(\hat{U} + \frac{\hat{\rho}\hat{g}\hat{h}^2\sin\alpha}{24\hat{\mu}}\right)(p,P), \quad \hat{p}_b = \frac{2\hat{\gamma}}{\hat{h}}p_b, \quad \hat{\kappa} = \frac{1}{\hat{R}}\kappa.
\end{aligned} \tag{B2}$$

The choice of this particular normalisation is not obvious in advance but we will see in due course that it simplifies the derived equation of motion for an isolated bubble. We note that (B2) reduces to the non-dimensionalisation used in §II when $\alpha = 0$ and $\hat{U} > 0$, and that we also recover the other extreme in which bubbles are purely buoyancy driven when $\hat{U} = 0$ and $\alpha > 0$.

We obtain the following dimensionless system:

$$\nabla^2 p = 0 \qquad \text{in} \quad \Omega, \tag{B3a}$$

$$p = P + 2(1-K)x \qquad \text{in} \quad \Omega, \tag{B3b}$$

$$p_b - \frac{3\mathrm{Ca}}{\epsilon}P = 1 + \mathrm{Ca}^{2/3}\beta(U_n)U_n^{2/3} + \frac{\epsilon\pi}{4}\kappa \qquad \text{on} \quad \partial\Omega_b, \tag{B3c}$$

$$\boldsymbol{n}\cdot\boldsymbol{\nabla}p = -U_n \qquad \text{on} \quad \partial\Omega_b, \tag{B3d}$$

$$p \sim -Kx + o(1) \qquad \text{as} \quad x^2+y^2 \to \infty. \tag{B3e}$$

The problem (B3) contains three dimensionless parameters: the aspect ratio, capillary number and velocity ratio, defined by

$$\epsilon = \frac{\hat{h}}{2\hat{R}}, \qquad \mathrm{Ca} = \frac{\hat{\mu}\hat{U}}{\hat{\gamma}K} = \frac{\hat{\mu}}{\hat{\gamma}}\left(\hat{U} + \frac{\hat{\rho}\hat{g}\hat{h}^2\sin\alpha}{24\hat{\mu}}\right), \qquad K = \frac{\hat{U}}{\hat{U} + \hat{\rho}\hat{g}\hat{h}^2\sin\alpha/24\hat{\mu}}, \tag{B4a–c}$$

respectively. The velocity ratio $K \in [0,1]$ allows us to interpolate between the limiting cases of a horizontal cell ($K = 1$) and a purely buoyancy-driven bubble ($K = 0$). As in §II, for the boundary-value problem (B3) to be valid, both ϵ and Ca must be small, and the dominant balance in the boundary condition (B3c), depends on the relative size of these two small parameters.

By integrating (B3c) around the bubble contour $\partial\Omega_b$ we derive the solvability condition

$$\oint_{\partial\Omega_b} -P\boldsymbol{n}\,\mathrm{d}s = \frac{\epsilon}{3\mathrm{Ca}^{1/3}} \oint_{\partial\Omega_b} \beta(U_n) U_n^{2/3} \boldsymbol{n}\,\mathrm{d}s, \tag{B5}$$

which corresponds to (8) and, again, may be interpreted as a force balance on the bubble. As in §II, it can be shown by symmetry that the bubble moves in the x-direction, with *a priori* unknown velocity U_b, say, and thus $U_n = U_b \boldsymbol{i} \cdot \boldsymbol{n}$.

b. Leading-order solution

In the distinguished limit where $\mathrm{Ca} = O(\epsilon^3)$, from (B3c) we find that the leading-order curvature is constant, so the bubble boundary is a unit circle to leading order. By defining polar coordinates (r, θ) based on the bubble centre, the leading-order problem can be solved using standard techniques to give

$$P = \left(\frac{U_b}{r} - 2r\right)\cos\theta - K\left(\frac{1}{r} - r\right)\cos\theta. \tag{B6}$$

The bubble velocity is then determined by the solvability condition (B5). Since the term in (B6) involving K is identically zero on the leading-order bubble boundary $r = 1$, the bubble velocity is independent of K and satisfies the algebraic equation

$$\frac{U_b^{2/3}}{2 - U_b} = \delta. \tag{B7}$$

By our choice of normalisation, U_b satisfies the same equation (27) as for a purely pressure-driven bubble, regardless of the value of K.

---

[1] S. L. Anna, Droplets and bubbles in microfluidic devices, Ann. Rev. Fluid Mech. **48**, 285 (2016).

[2] A. Huerre, V. Miralles, and M.-C. Jullien, Bubbles and foams in microfluidics, Soft Matter **10**, 6888 (2014).

[3] V. Gnyawali, B. U. Moon, J. Kieda, R. Karshafian, M. C. Kolios, and S. S. H. Tsai, Honey, I shrunk the bubbles: microfluidic vacuum shrinkage of lipid-stabilized microbubbles, Soft Matter **13**, 4011 (2017).

[4] T. Beatus, R. H. Bar-Ziv, and T. Tlusty, The physics of 2D microfluidic droplet ensembles, Phys. Rep. **516**, 103 (2012).

[5] P. Garstecki, I. Gitlin, W. DiLuzio, G. M. Whitesides, E. Kumacheva, and H. A. Stone, Formation of monodisperse bubbles in a microfluidic flow-focusing device, Appl. Phys. Lett **85**, 2649 (2004).

[6] B. Reichert, A. Huerre, O. Theodoly, M.-P. Valignat, I. Cantat, and M.-C. Jullien, Topography of the lubrication film under a pancake droplet travelling in a Hele-Shaw cell, J. Fluid Mech. **850**, 708 (2018).

[7] G. Taylor and P. G. Saffman, A note on the motion of bubbles in a Hele-Shaw cell and porous medium, Q. J. Mech. Appl. Math. **12**, 265 (1959).

[8] S. Tanveer, The effect of surface tension on the shape of a Hele-Shaw cell bubble, Phys. Fluids **29**, 3537 (1986).

[9] C. C. Green, C. J. Lustri, and S. W. McCue, The effect of surface tension on steadily translating bubbles in an unbounded Hele-Shaw cell, Proc. R. Soc. Lond. A **473**, 20170050 (2017).

[10] C. J. Lustri, C. C. Green, and S. W. McCue, Selection of a Hele-Shaw bubble via exponential asymptotics, SIAM J. Appl. Math. **80**, 289 (2020).

[11] A. Gaillard, J. Keeler, G. Le Lay, G. Lemoult, A. Thompson, A. Hazel, and A. Juel, The life and fate of a bubble in a geometrically perturbed Hele-Shaw channel, J. Fluid Mech. **914**, A34 (2021).

[12] J. S. Keeler, A. B. Thompson, G. Lemoult, A. Juel, and A. L. Hazel, The influence of invariant solutions on the transient behaviour of an air bubble in a Hele-Shaw channel, Proc. R. Soc. Lond. A **475**, 20190434 (2019).

[13] A. Franco-Gómez, A. B. Thompson, A. L. Hazel, and A. Juel, Bubble propagation in Hele-Shaw channels with centred constrictions, Fluid Dyn. Res. **50**, 021403 (2018).

[14] F. Bretherton, The motion of long bubbles in tubes, J. Fluid Mech. **10**, 166 (1961).

[15] C.-W. Park and G. M. Homsy, Two-phase displacement in Hele-Shaw cells: theory, J. Fluid Mech. **139**, 291 (1984).

[16] E. Meiburg, Bubbles in a Hele-Shaw cell: Numerical simulation of three-dimensional effects, Phys. Fluids A **1**, 938 (1989).

[17] D. Burgess and M. R. Foster, Analysis of the boundary conditions for a Hele-Shaw bubble, Phys. Fluids A **2**, 1105 (1990).

[18] M. Nagel, *Modeling droplets flowing in microchannels*, Ph.D. thesis (2014).

[19] D. J. Booth, I. M. Griffiths, and P. D. Howell, Circular bubbles in a Hele-Shaw channel: a Hele-Shaw Newton's cradle, J. Fluid Mech. **954**, A21 (2023).

[20] T. Maxworthy, Bubble formation, motion and interaction in a Hele-Shaw cell, J. Fluid Mech. **173**, 95 (1986).

[21] A. Eri and K. Okumura, Viscous drag friction acting on a fluid drop confined in between two plates, Soft Matter **7**, 5648 (2011).

[22] B. Monnet, C. Madec, V. Vidal, S. Joubaud, and J. J. S. Jerome, Bubble rise in a Hele-Shaw cell: bridging the gap between viscous and inertial regimes, J. Fluid Mech. **942**, R3 (2022).

[23] D. Halpern and O. E. Jensen, A semi-infinite bubble advancing into a planar tapered channel, Phys. Fluids **14**, 431 (2002).

[24] H. Wong, C. J. Radke, and S. Morris, The motion of long bubbles in polygonal capillaries. Part 2. Drag, fluid pressure and fluid flow, J. Fluid Mech. **292**, 95 (1995).

[25] V. Suresh and J. B. Grotberg, The effect of gravity on liquid plug propagation in a two-dimensional channel, Phys. Fluids **17**, 031507 (2005).

[26] A. De Ryck and D. Quéré, Inertial coating of a fibre, J. Fluid Mech. **311**, 219 (1996).

[27] A. Q. Shen, B. Gleason, G. H. McKinley, and H. A. Stone, Fiber coating with surfactant solutions, Phys. Fluids **14**, 4055 (2002).

[28] G. G. Peng, D. Pihler-Puzović, A. Juel, M. Heil, and J. R. Lister, Displacement flows under elastic membranes. Part 2. Analysis of interfacial effects, J. Fluid Mech. **784**, 512 (2015).

[29] L. C. Morrow, C. Cuttle, and C. W. MacMinn, Gas compression systematically delays the onset of viscous fingering, Phys. Rev. Lett. **131**, 224002 (2023).

[30] D. A. Reinelt and P. G. Saffman, The penetration of a finger into a viscous fluid in a channel and tube, SIAM J. Comput. **6**, 542 (1985).